Journal of Alloys and Compounds 1010 (2025) 177825

Contents lists available at ScienceDirect

Journal of Alloys and Compounds

journal homepage: www.elsevier.com/locate/jalcom

Grain size dependence of deformation behavior in Ti–15Mo alloy prepared by powder metallurgy

Chenyang Wu [a], Xiaoli Zhao [a,b,c,*], Takayoshi Nakano [d], Mitsuo Niinomi [d,e], Nan Jia [a], Deliang Zhang [a]

[a] School of Materials Science and Engineering, Northeastern University, Shenyang 110819, PR China
[b] National Frontiers Science Center for Industrial Intelligence and Systems Optimization, Northeastern University, Shenyang 110819, PR China
[c] Key Laboratory of Data Analytics and Optimization for Smart Industry (Ministry of Education), Northeastern University, Shenyang 110819, PR China
[d] Division of Materials and Manufacturing Science, Graduate School of Engineering, Osaka University, 2-1, Yamadaoka, Suita, Osaka 565-0871, Japan
[e] Institute for Materials Research, Tohoku University, Sendai, Miyagi 980-8577, Japan

ARTICLE INFO

Keywords:
Ti–Mo alloy
Power metallurgy
Grain refinement
Mechanical properties
Mechanical twinning

ABSTRACT

To the best of our knowledge, this is the first report demonstrating grain refinement to 4 μm via a mass-production method for the Ti–15Mo alloy. Grain sizes ranging from 4 to 38 μm were achieved by controlling thermomechanical processing in powder metallurgy, combined with heat treatment using recycled coarse powders for additive manufacturing. The critical grain size for deformation twinning was investigated, alongside an analysis of the deformation behavior and mechanical properties of the Ti–15Mo alloy with various grain sizes. Upon refining the grain size to 7 μm, deformation twinning is inhibited, shifting the plastic deformation mechanism from mechanical twinning to dislocation slip. The yield strength can be adjusted between 921 and 715 MPa, with elongation ranging from 18.4 % to 34.4 %, by varying the grain size distribution ratio of small to large grains relative to 7 μm from 1.5 to 0.42. This strengthening effect primarily arises from dislocation strengthening, Mo solid solution, texture strengthening, and modifications in the Hall-Petch constant due to changes in deformation behavior during grain refinement.

1. Introduction

β titanium alloys have garnered considerable attention in biomedical applications due to their excellent biocompatibility and low elastic modulus, which is closer to that of bone (10–30 GPa). Molybdenum (Mo), a common stabilizing element, forms a solid solution with titanium, causing minimal lattice distortion [1]. Additionally, Mo contributes to grain refinement and increase the strength of the alloys. As Mo content increases from 9 to 15 wt%, the β stability increases, and the plastic deformation mechanism shifts from α'' martensite and ω phase transformation to {332}<113> and {112}<111> mechanical twinning [2]. The Ti–15Mo alloy, a β-type titanium alloy listed in ASTM standards as an implant material [3], is widely used in biomedical fields due to its excellent corrosion resistance and biocompatibility. However, its low yield strength limits broader practical applications. This low yield strength is attributed to the low critical stress required for mechanical twinning, making yield strength enhancement highly significant. A combination of dislocation slip and mechanical twinning can achieve excellent mechanical properties in Ti–15Mo alloys [4]. The addition of elements such as Fe shifts the deformation mode from {332}<113> twinning to dislocation slip, significantly increasing the yield strength of the alloy [5]. However, altering the alloy's standardized chemical composition poses challenges in securing production licenses for biomedical applications. Furthermore, while second phase strengthening and dislocation strengthening can enhance yield strength, they often reduce ductility. The second phases, typically including the ω and α phases, are detrimental to maintaining a low Young's modulus, which is crucial for minimizing the stress shielding effect [6–10]. Grain refinement is a critical strategy for enhancing yield strength without increasing Young's modulus. In metastable alloys, grain refinement enhances β phase stability, leading to an increase in the critical stress required for twinning or deformation-induced phase transformations, thereby improving the yield strength of materials. Numerous studies have shown that deformation twinning is suppressed in materials with hexagonal close-packed (HCP) or face-centered cubic (FCC) structures when the grain size is reduced to a few micrometers [11–14]. However,

* Corresponding author at: School of Materials Science and Engineering, Northeastern University, Shenyang 110819, PR China.
E-mail address: zhaoxl@mail.neu.edu.cn (X. Zhao).

https://doi.org/10.1016/j.jallcom.2024.177825
Received 22 August 2024; Received in revised form 23 November 2024; Accepted 27 November 2024
Available online 28 November 2024

the body-centered cubic (BCC) structure of titanium alloys makes micron-scale grain refinement particularly challenging due to rapid diffusion at high temperatures in the non-close-packed structure. Although techniques such as accumulative roll bonding (ARB), equal channel angular pressing (ECAP), high-pressure torsion (HPT), and other severe plastic deformation methods combined with heat treatments can effectively achieve grain refinement, scaling these methods for mass production remains a significant challenge. Selective laser melting, characterized by its fast cooling rate, effectively increase the yield strength to 728 MPa. This improvement is attributed to the irregularly refined grain size of 15 μm and the formation of the dislocation walls accompanied by element segregation [15]. To the best of our knowledge, deformation twinning is the predominant deformation mechanism in Ti–15Mo alloys with varying grain sizes, as reported in existing studies. However, determining the critical grain size at which the deformation mode transitions from twinning to dislocation slip remains a pivotal question for optimizing the alloy's mechanical properties [15–18]. The in-house thermomechanical consolidation method in powder metallurgy is a near-net-shape forming process that allows precise microstructural control during fabrication. This cost-effective and time-efficient approach enables the production of dense materials with refined grain structures and is particularly advantageous for recycling coarse powders from additive manufacturing through a streamlined and efficient process [19,20]. This paper investigates the feasibility of fabricating dense Ti–15Mo alloy with low oxygen content and refined grain size through powder metallurgy, utilizing recycled coarse powders from additive manufacturing. It further aims to identify the grain size threshold for the transition of plastic deformation modes and to regulate the alloy's deformation mechanism by controlling grain size and its distribution, thereby enhancing its mechanical properties.

2. Materials and methods

2.1. Materials

Spherical Ti–15Mo pre-alloyed powders, with a powder refractive index of 2.8, were used as the raw material. As shown in Fig. 1, the particle size of the powders was measured using a laser particle size distribution meter (LA-920), and the average particle size is 145 μm. The Ti–15Mo alloy was fabricated through a thermomechanical powder metallurgy process (Fig. 2a) under an argon atmosphere. As shown in Fig. 2b-c, the powders were first cold compacted into a cylinder with a diameter of 52 mm and a height of 30 mm first to preform the material. Subsequently, the preformed cylinder was hot extruded into a rod with a diameter of 18 mm and a true strain of 2.20 at 1200 °C. The extruded materials were analyzed for interstitial element content using a gas chromatograph (SQM-2 L) with chromatographic separation and detection techniques. The measured mass percentages of hydrogen (H), oxygen (O) and nitrogen (N) were 0.013 %, 0.075 % and 0.033 %, respectively, meeting the requirements of ASTM standards. The material densification was assessed using an electronic density balance (ETNALN, ET-320) in accordance with Archimedes' method. The calculation formula is as follows:

$$\theta = \left(1 - \frac{\rho_0}{\rho_1}\right) * 100\% \quad (1)$$

$$\rho_0 = \left(\frac{m_1 * 1.103}{m_3 - m_2}\right) \quad (2)$$

$$\rho_t = \left(\frac{1}{\sum_i^n \frac{m_i}{\rho_i}}\right) \quad (3)$$

Where θ is the porosity of the material, ρ_0 is the experimental density of the materials, ρ_t is the theoretical density of the material, and ρ_i is the theoretical density of each element. m_1, m_2, and m_3 are the dry weights of the material, the weight of material in water, and the weight of wet material removed from the water, respectively, and m_i is the mass fraction of each alloying element. By averaging ten measurements, the measured density of the as-extruded Ti–15Mo material was 4.94 g/cm^3, achieving a densification of 99.8 %. To produce Ti–15Mo materials with varying grain sizes, the samples were heat-treated at temperatures ranging from 765 to 800 °C for durations of 2–40 minutes, followed by ice-water quenching.

2.2. Methods

Tensile specimens with dimensions of 40 mm in total length, a parallel segment of 13 mm, a width of 3 mm, and a thickness of 1.5 mm were prepared using electrical discharge machining (EDM) wire cutting. Tensile tests were conducted at room temperature with a strain rate of 3×10^{-4} s^{-1} using a Shimadzu AG-XPLUS 100 kN tensile testing machine. To minimize errors, at least three parallel specimens were prepared for each material with different grain sizes. Prior to optical microscopy (OM) observation using a ZESS AXIO optical microscope, the specimens were mechanically polished and chemically etched with a solution composed of 2 % hydrofluoric acid (HF), 4 % nitric acid (HNO_3), and 94 % distilled water (H_2O). Grain size analysis was performed using ImageJ software, counting more than 1000 grains, with at least three regions analyzed to ensure accuracy and reduce measurement error.

The phase constitutions and lattice constants of the materials, both before and after tensile deformation, were analyzed using X-ray diffractometry (XRD, Smart Lab). Scanning electron microscopy (SEM, JEOL JSM-7001F) and EBSD (EBSD detector, BRUKER e-Flash FS) were employed to investigate the deformation products and texture intensity of the materials with varying grain sizes. The EBSD analysis was

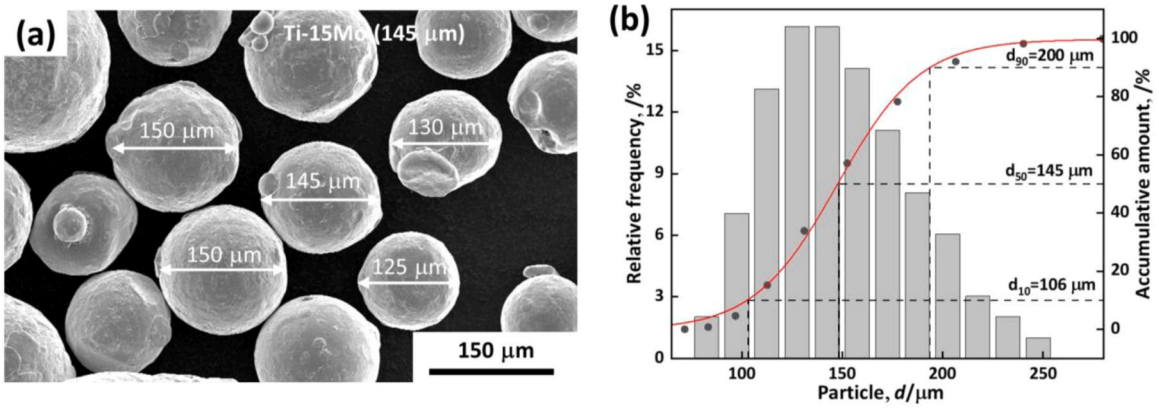

Fig. 1. (a) SEM image showing the morphology of Ti–15Mo pre-alloyed powders and (b) the particle size distribution of the powders.

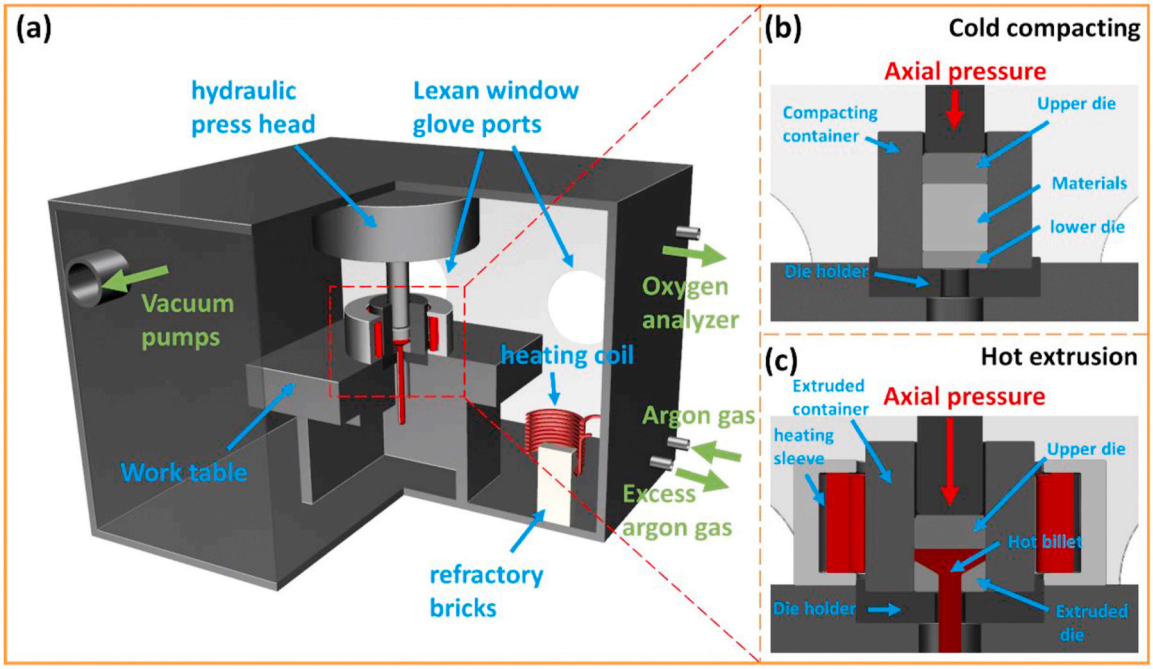

Fig. 2. (a) Schematic of thermomechanical equipment used in powder metallurgy, (b) cold compaction process for powders, and (c) hot extrusion process.

conducted with a step size set to one-fifth of the smallest microstructural feature in the selected area, using an electron beam at 20 kV and 26 nA. For EBSD analysis, the samples were electropolished using a Zhaoxin RXN-605D power supply with a voltage of 27 V, a current of 0.8–1 A, and a temperature of −10 °C. The electrolyte consisted of 5 vol% perchloric acid, 35 vol% n-butyl alcohol, and 60 vol% methyl alcohol.

3. Result

3.1. Microstructure

Fig. 3 presents the optical micrographs of Ti–15Mo materials after various treatment processes. The materials with different grain sizes exhibit equiaxed grains alongside some extruded microstructure. As shown in Fig. 3a, equiaxed grains with an average grain size of 4 μm was obtained through the thermomechanical powder metallurgical process. Average grain sizes of 7 μm and 13 μm were achieved through short-time heat treatments (2 min and 10 min) at 765 °C (β phase transformation

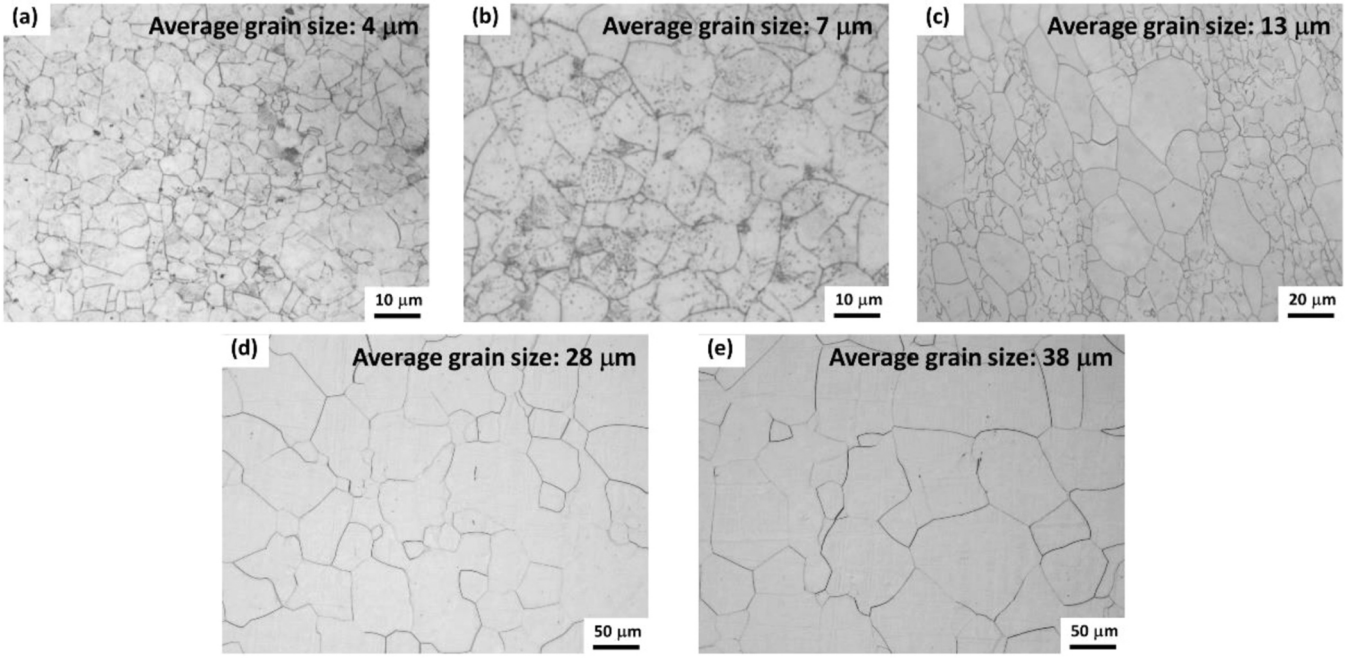

Fig. 3. Metallographic images of Ti–15Mo alloy subjected to various heat treatment conditions, including different temperatures and holding times: (a) as-extruded, (b) 765 °C for 2 minutes, (c) 765 °C for10 minutes, (d) 800 °C for 30 minutes, and (e) 800 °C for 40 minutes.

temperature +10 °C), with both exhibiting a mixture of coarse and fine grains (Fig. 3b–c). Heat treatments at 800 °C for 30 min. and 40 min. result in average grain sizes of 28 μm and 38 μm, respectively. The results demonstrate that the coarse Ti–15Mo powders with an initial average powder size of 145 μm can be densely consolidated through a thermomechanical process, achieving a refined grain size of 4 μm. Additionally, the grain size of Ti–15Mo materials can be tailored within the range of 4–38 μm by adjusting the parameters of post-processing heat treatments. Fig. 4a illustrates the phase constitutions of Ti–15Mo materials with varying grain sizes, indicating that all materials are predominantly composed of β phases. The solution treatment was performed above the β transus temperature for a short duration to minimize excessive grain growth. Due to air cooling following hot extrusion, a small number of α additional peaks, aside from β peaks, are observed in the XRD patterns. However, their negligible content and minimal impact on material properties render them insignificant for detailed discussion. Fig. 4b shows that the lattice constant of the materials fluctuates between 3.2605 and 3.2655 Å. Residual stresses introduced during hot extrusion are released during heat treatment, leading to variations in the lattice constant as the grain size increases from 4 to 38 μm.

3.2. Mechanical properties and fractography

Fig. 5a displays the engineering stress-strain curves of Ti–15Mo materials with varying grain sizes. As the average grain size increases from 4 to 38 μm, the yield strength decreases from 1118 to 592 MPa, and the ultimate tensile strength declines from 1119 to 811 MPa. Conversely, the elongation improves significantly, rising from 13.2 % to 40 %. For materials with grain size of 7 μm and 13 μm, the comprehensive mechanical properties include yield strengths of 921 and 715 MPa, and elongation values of 18.4 % and 34 %, respectively. These results demonstrate the trade-off between strength and ductility with varying grain sizes. As shown in Fig. 5b, the grain size of Ti–15Mo alloy can be effectively controlled through powder metallurgy via thermomechanical consolidation and heat treatment, resulting in excellent mechanical properties. By incorporating additional strengthening and toughening strategies, such as the introduction of oxygen (O) and boron (B) or the incorporation of isothermal ω phase through ageing, it is anticipated that the already excellent performance of the 13 μm and 7 μm materials can be further enhanced [15,21–30].

Fig. 6(a–b) presents the true stress-strain curves and work-hardening curves of Ti–15Mo materials with varying grain sizes. The results show that the material with grain size of 4 μm exhibits high strength but almost no work-hardening ability. In contrast, materials with grain size larger than 13 μm demonstrate better work-hardening capability. For the material with grain size of 7 μm, some work-hardening ability is observed, and the uniform elongation increases from 1.2 % (in the 4 μm material) to 5.8 %. As summarized in Table 1, an increase in average grain size leads to a decrease in strength but an improvement in ductility. Specifically, as the grain size increases from 4 μm to 38 μm, the area reduction improves from 0.41 to 0.71, the yield strength and tensile strength decrease from 1118 and 1119 MPa to 592 MPa and 811 MPa, respectively, while the elongation increase significantly from 13.2 % to 40 %, and the uniform elongation rises from 1.2 % to 22.1 %.

The tensile fractography of Ti–15Mo materials with different grain sizes, as shown in Fig. 7(a–d), reveals a combination of ductile and ductile-brittle mixed fracture areas. In the ductile fracture area, numerous dimples are observed, exhibiting a typical ductile fracture morphology (Fig. 7a′–d′). In the ductile-brittle mixed fracture area (Fig. 7a″–d″), in addition to dimples, a significant number of cleavage fracture features are present, presenting a mixed fracture morphology. The proportion of the ductile fracture area increases notably from 15 % to 75 % as the grain size increases from 4 μm to 28 μm. This trend confirms that a larger ductile fracture area ratio correlates with greater ductility in the materials [31].

Additionally, cracks are observed on the fracture surface, prompting an analysis of their origins through observations of the longitudinal section of the material. For the 13 μm material, as shown in Fig. 8a, numerous cracks are visible in the longitudinal section of the tensile fracture at 34 % strain. In contrast, near the fracture surface at 17 % strain (Fig. 8b), only a few cracks are observed, and no significant cracks are present far from the fracture surface at 0 % strain (Fig. 8c). This suggests that the cracks at the fracture surface are generated during the tensile deformation process rather than during fabrication. In the 28 μm material, which undergoes substantial plastic deformation, a similar pattern is observed. A large number of cracks are present at the fracture surface at 40 % strain, whereas only microcracks are observed near the fracture surface at 20 % strain (Fig. 8d–e). Fig. 8(a, d, f) shows that as the grain size decreases from 28 μm to 4 μm, the size and number of cracks formed during deformation significantly reduce. This highlights the influence of grain size on crack formation during the deformation process.

Furthermore, the size of cracks at similar strain levels is comparable across materials with different average grain sizes, allowing the strain to be evaluated using a crack growth model. As applied stress increases, stress concentration arises from dislocation pile-ups at grain boundaries, leading to the initiation of microcracks at triple grain junctions. These microcracks progressively grow with increasing strain, ultimately forming visible cracks.

With increasing grain size, mechanical twinning occurs to accommodate deformation, enabling higher strain levels. This increase in strain elevates the kinetic energy available for microcrack propagation

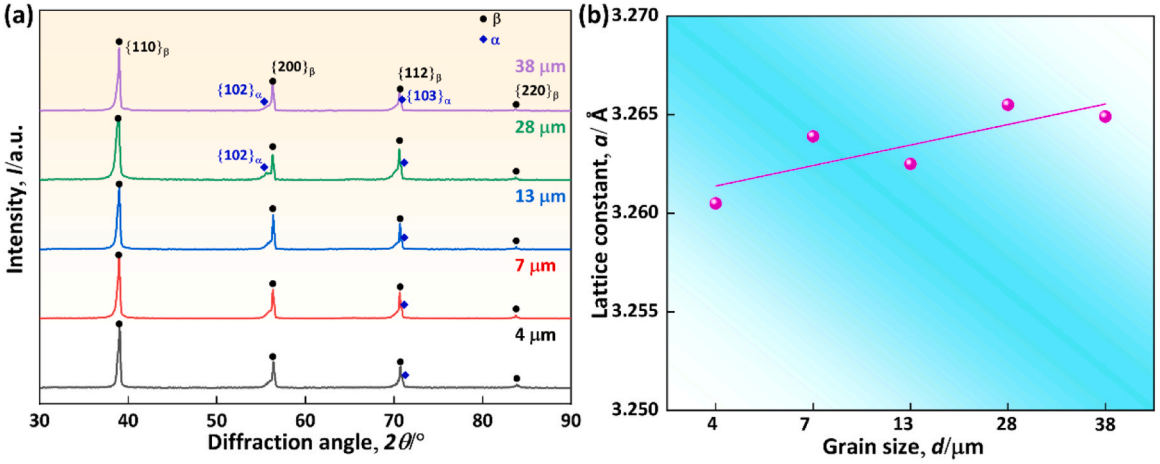

Fig. 4. (a) XRD patterns of materials with different grain sizes and (b) lattice constants of the β phase in materials as a function of grain size.

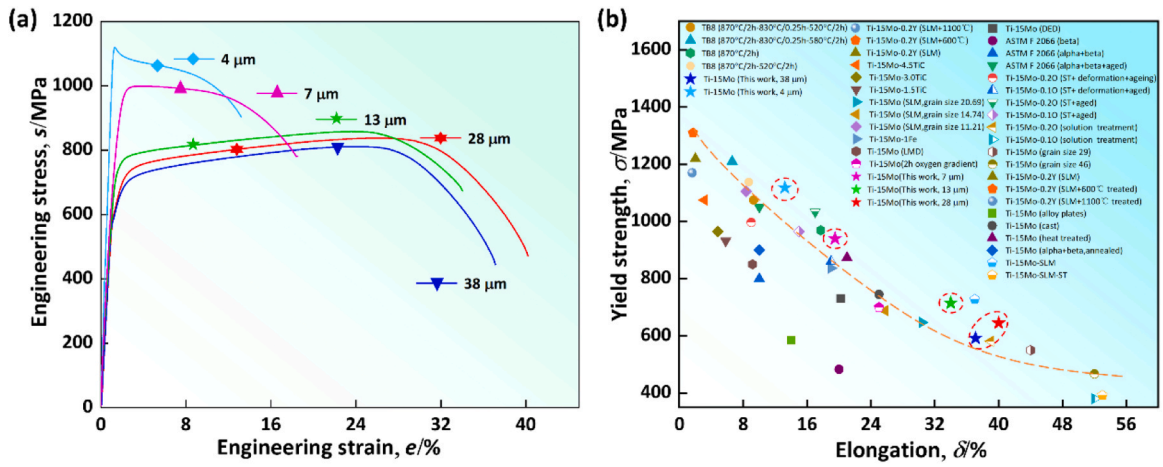

Fig. 5. (a) Engineering stress-strain curves of Ti–15Mo materials with varying grain sizes and (b) yield strength-elongation relationship for common Ti–15Mo-based alloys [6,21–30].

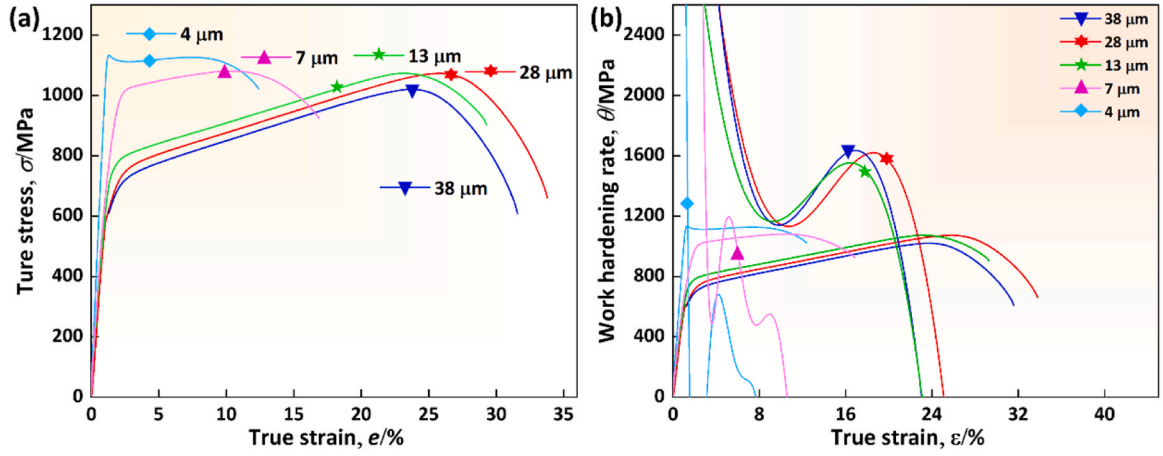

Fig. 6. (a) True stress-strain curves and (b) work-hardening rate curves of Ti–15Mo materials with varying grain sizes.

Table 1
Tensile properties of Ti–15Mo materials with different grain sizes.

Grain size	Area reduction	Yield strength /MPa	Ultimate tensile strength /MPa	Total elongation (%)	Uniform elongation (%)
38 μm	0.71	592±7	811±79	37.1±2.3	21.0±0.5
28 μm	0.68	645±37	854±17	40±0.2	22.1±0.6
13 μm	0.48	715±12	858±13	34.0±1.5	20.5±0.4
7 μm	0.48	921±19	998±71	18.4±5.4	5.8±0.3
4 μm	0.41	1118±31	1119±30	13.2±3.3	1.2±0.5

under plastic deformation, facilitating full microcrack extension into larger cracks. The role of plastic strain in microcrack growth is primarily attributed to the formation of microcrack barriers under plastic deformation and the necking effect at the tensile fracture, which reduces the working volume and further influences crack [32,33].

As shown in Fig. 9, the hardness of Ti–15Mo materials decreases from 359 to 288 HV as the grain size increases from 4 to 13 μm. Hardness, which reflects a material's ability to resist localized deformation, typically decreases with increasing grain size due to the Hall-Petch effect [34,35]. However, when the grain size increases beyond 13 μm, the hardness rises to 320 HV. This increase may be attributed to a change in the deformation behavior of the material, shifting to mechanical twinning as the grain size grows larger. Notably, pronounced twinning is observed near the indentations in large-grain materials, as shown in the inset of Fig. 9, which further supports the role of mechanical twinning in influencing the hardness of materials with larger grains.

4. Discussion

4.1. Microstructure

The grain size of metallic materials can be refined during hot deformation [36,37]. As illustrated in Fig. 10a, the Ti–15Mo alloy exhibits numerous sub-grain boundaries. The KAM (Fig. 10b) reveals that these sub-grain boundaries, along with high dislocation density grain boundaries, continuously absorb dislocations. Furthermore, as shown in Fig. 10c, dynamic recrystallization during in-house thermomechanical consolidation facilitates the progressive absorption of dislocations by the sub-grain boundaries. This process increases the grain boundary misorientation, transforming low-angle grain boundaries into high-angle grain boundaries, thereby refining the Ti–15Mo alloy grain size to be 4 μm [38,39]. The deformation mode significantly influences the mechanical properties of materials. Fig. 11(a–b) presents the optical micrographs of Ti–15Mo materials with average grain sizes of 4 and 28 μm after deformation. In the material with a 4 μm average grain size (Fig. 11a), no lath structures are formed during deformation. Conversely, the material with a 28 μm average grain size (Fig. 11b) exhibits a significant amount of lath structures after tensile deformation.

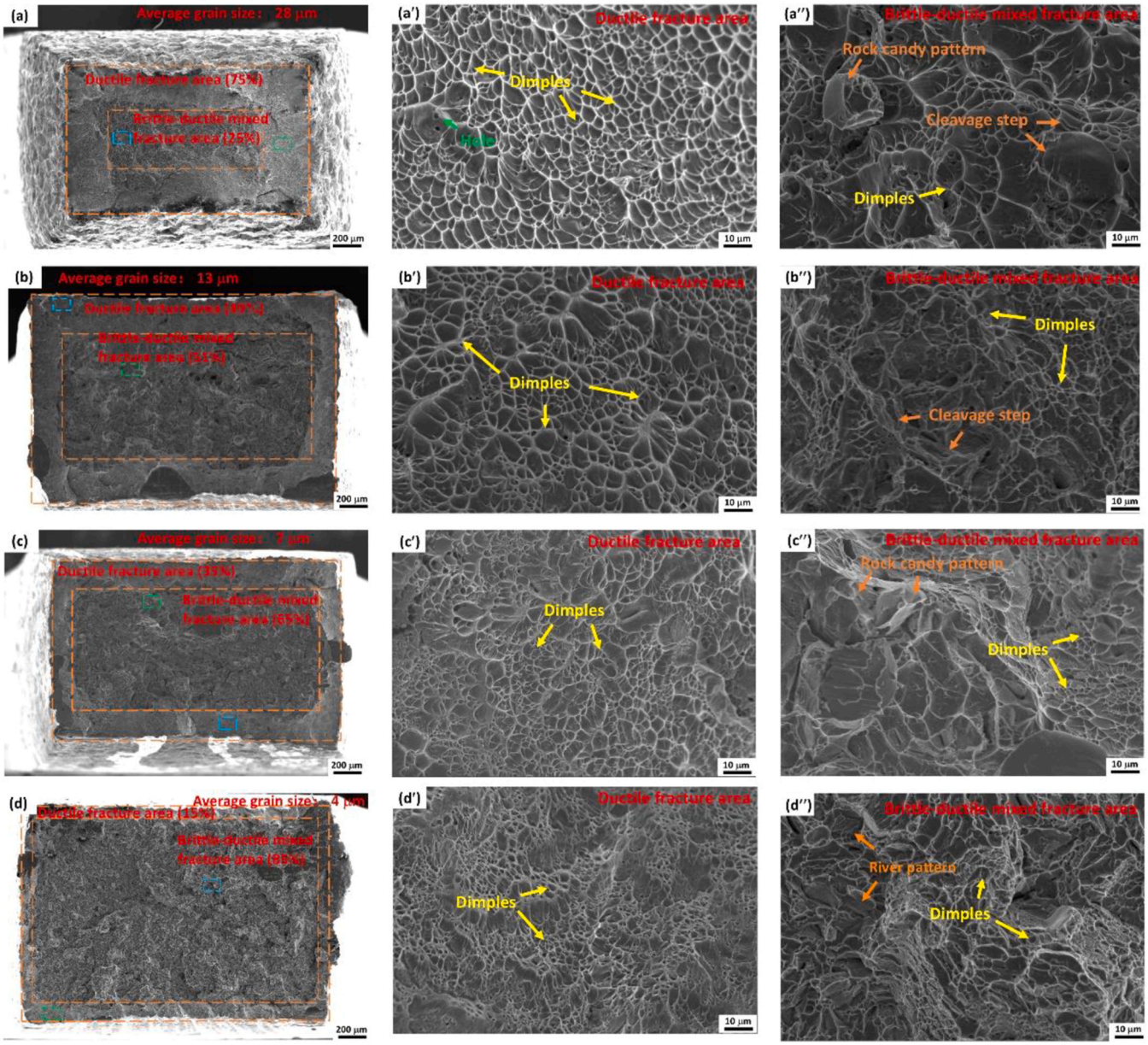

Fig. 7. (a–d) Tensile fractography of Ti–15Mo materials with varying grain sizes illustrating the SEM images of the ductile fracture area (a′–d′) and ductile-brittle mixed fracture area (a″–d″). Grain sizes: (a) 28 μm, (b) 13 μm, (c) 7 μm, and (d) 4 μm.

For the material with a 7 μm average grain size (Fig. 11c), lath structures are observed only in larger grains. Statistical analysis indicates that lath structures are predominantly observed in grains larger than 7 μm, as marked with red indicators in the micrographs. In contrast, no prominent lath structures are detected in grains smaller than 7 μm, as denoted by yellow markers. This observation highlights the grain size threshold for the formation of lath structures during deformation. From Fig. 11d, the deformed material with a lath structure is primarily composed of β phase. In Ti–15Mo alloy, the lath structure formed during deformation is predominantly attributed to twinning [40,41]. Therefore, it is inferred that the lath structure consists of deformation twins or kinks.

To exclude the effect of the Schmid factor on the grain size dependency of the statistically deformed lath structure, the Schmid factor distribution in the 7 μm material was analyzed using EBSD. As shown in Fig. 12(a–b), most grains in the observed area exhibit a Schmid factor greater than 0.4, and the lath structure is identified as {332}<113> deformation twinning. However, no noticeable mechanical twins are observed in smaller grains, despite having similarly high Schimid factors as the larger grains. Statistical analysis determines the critical grain size that hinders deformation twinning to be 7 μm. This critical grain size enables an optimal balance between strength and ductility in Ti–15Mo alloy, particularly in materials with average grain sizes of 7 μm and 13 μm.

In many metallic materials, twinning is progressively suppressed as the grain size decreases [12,14,42–44]. However, when the grain size reaches the threshold of twin suppression, the deformation behavior of the material undergoes significant changes. As illustrated in Fig. 13a, when the material is subjected to loading, dislocation pile-ups near the grain boundaries as applied stress increases. In materials with smaller grain size, the distance between the dislocation source and the grain boundaries is reduced, resulting in fewer pile-up dislocations. Consequently, local stress concentration is lower, and more evenly distributed at the fine grain boundaries, requiring higher external stresses for dislocation multiplication. Fig. 13b shows that Ti–15Mo materials with a body-centered cubic structure possess multiple slip planes, including {110}, {112}, and {123}, with a stable <111> slip direction.

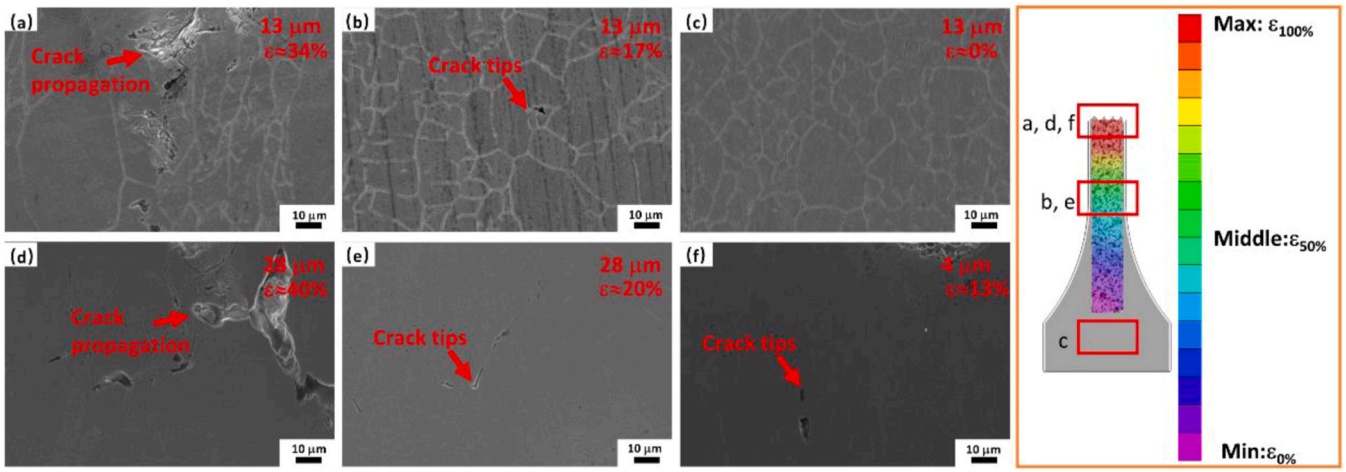

Fig. 8. (a–f) SEM images of tensile longitudinal sections of Ti–15Mo alloy materials with varying grain sizes, captured at different locations: (a, d, f) at the fracture surfaces (a: d=13μm, ε=34 %; d: d=28μm, ε=40 %; f: d=4μm, ε=13 %); (b, e) near the fracture surfaces (b: d=13μm, ε=17 %; e: d=28μm, ε=20 %); (c) away from the fracture surfaces (c: d=28μm, ε=0 %).

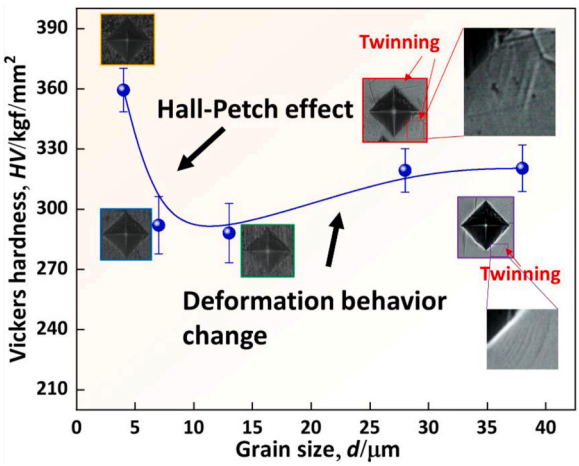

Fig. 9. Variation in Vickers hardness of Ti–15Mo materials as a function of average grain size.

Dislocations are continuously generated through the Frank-Read (FR) dislocation source. As shown in Fig. 13c, grain boundaries acts as critical barriers to dislocation slip. In materials with small grain size, a higher proportion of grain boundaries leads to increased dislocation interactions and pile-ups at these boundaries. This accumulation can initiate crack nucleation, causing cracks to grow or expand across the grain boundaries, ultimately resulting in material failure. With increasing grain size (Fig. 13d), the distance between the dislocation source and the grain boundaries increases, allowing more dislocations to pile up. This raises the stress exerted by the leading dislocations on the grain boundary barriers. When this stress reaches the critical level, mechanical twinning is initiated. As illustrated in Fig. 13e, interactions between grain boundaries and dislocations under high stress concentration facilitate {332}<113> twinning (indicated by yellow arrows) through atomic shear movement (green arrows). This twinning alters the grain orientation, transforming an originally unfavorable orientation for slip into a favorable one, further promoting dislocation slip. The crystallographic misorientation between the {332}<113> twins and the matrix is 50.5°, with rotation along the <011> axis (Fig. 13f).

4.2. Strengthening mechanism

The deformation behavior and mechanical properties of Ti–15Mo alloys are influenced by variations in grain size, necessitating a detailed investigation into the extent of these changes to enable further material optimization. To quantitatively analyze the factors affecting the mechanical properties, Eq. (4) examines the contributions of solid solution strengthening, dislocation strengthening, grain refinement strengthening, texture, and other mechanisms to the yield strength of the material.

$$\sigma = \sigma_0 + \Delta\sigma_{ss} + \Delta\sigma_d + \Delta\sigma_g + \sigma_{tando} \tag{4}$$

where σ_0 represents the yield strength of pure Ti, taken as 250 MPa[45], $\Delta\sigma_{ss}$ denotes the contribution from solid solution strengthening of Mo, $\Delta\sigma_d$ represents the contribution from dislocation strengthening, $\Delta\sigma_g$ accounts for the contribution from grain refinement strengthening, and $\sigma_{t\ and\ o}$ captures the contribution from texture and other strengthening mechanism.

The dislocation density of the materials increases significantly after hot extrusion, effectively impeding dislocation movement and enhancing the strength of the materials. The contribution of dislocation strengthening is quantified using the Taylor equation [46,47]:

$$\Delta\sigma_d = M\alpha Gb\rho^{0.5} \tag{5}$$

Here, M is the Taylor factor, set to 3.06, α represents the dislocation strengthening coefficient for titanium, with a value of 0.25, G and b are the shear modulus and Burgers vector of titanium alloy, with respective values of 52 GPa and 2.86 Å. The dislocation density ρ is determined using the Williamson-Hall formula based on XRD results [48,49].

Solid solution strengthening arises from the alloying elements such as Mo. The size and shear modulus mismatch between the solute atoms (Mo) and the matrix Ti atoms induces lattice distortion, thereby increasing the strength of the alloy. The content of interstitial solid solution atoms (H, O and N) in the studied materials conform to ASTM standards and show no significant variation among the materials; hence, the strengthening effect of interstitial atoms is considered negligible. The contribution of solid solution strengthening is quantified using Fleischer's model to calculate the increase in strength, denoted as $\Delta\sigma_{ss}$[50,51] :

$$\Delta\sigma_{ss} = MGb\varepsilon_{ss}c^{\frac{1}{2}} \tag{6}$$

$$\varepsilon_{ss} \approx \left| \frac{\varepsilon_G}{1 + \frac{1}{2}|\varepsilon_G|} - 3 \bullet \varepsilon_a \right| \tag{7}$$

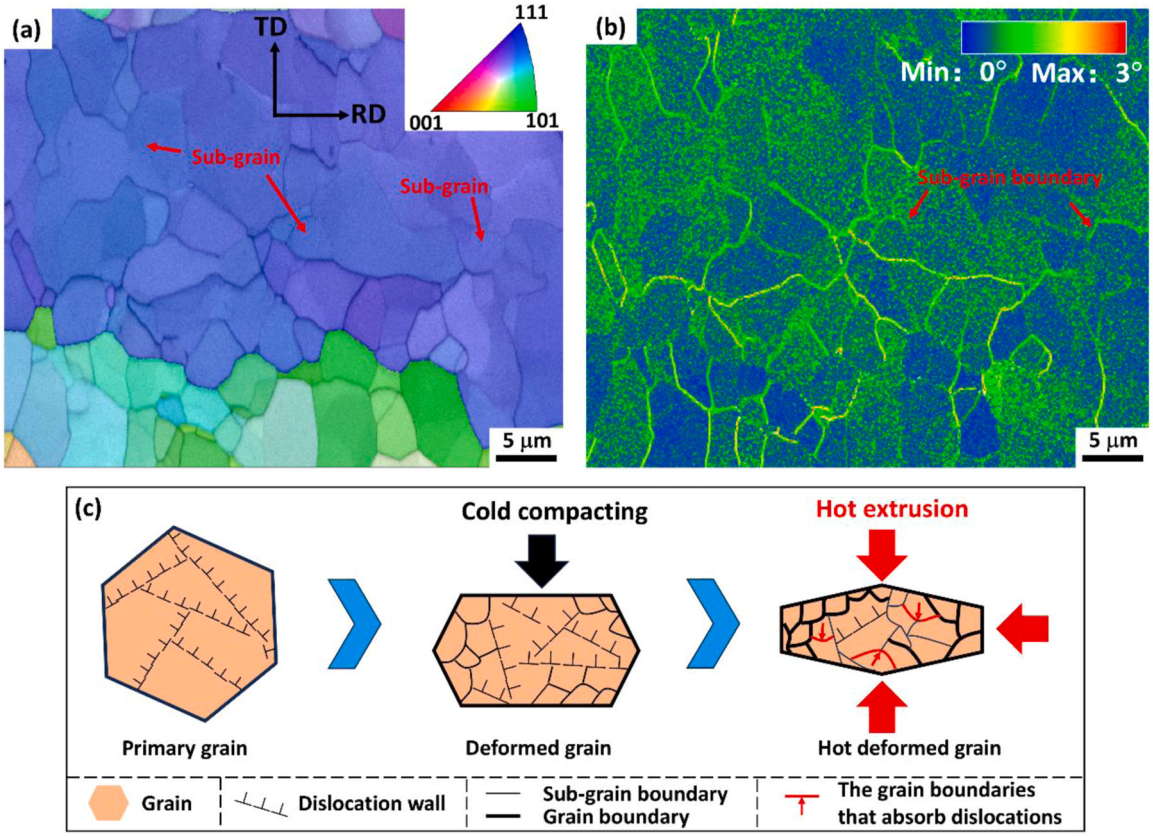

Fig. 10. (a) Inverse Pole Figure (IPF) map and (b) Kernel Average Misorientation (KAM) map of Ti–15Mo material with an average grain size of 4 μm, and (c) diagram of grain refinement during thermomechanical consolidation.

Where M is the Taylor factor, taken as 3.06, G is the shear modulus, b is the Burgers vector, and c is the atomic percent of the Mo solute. ε_G and ε_a represent the lattice strain resulting from the difference in shear modulus and atomic dimensions between the solutes and the matrix, with values of 2.063 and 2.669, respectively. Based on this model, the calculated contribution of solid solution strengthening to the yield strength is approximately 164 MPa.

Grain refinement increases material strength by providing dense grain boundaries that impede dislocation motion. This effect is typically quantified using the Hall-Petch equation [52] :

$$\sigma_y = \sigma_0 + \mathrm{k}d^{-\frac{1}{2}} \tag{8}$$

Where σ_y is the yield strength of the material, σ_0 represents the intrinsic lattice resistance to dislocation movement, k is the Hall-Petch coefficient, which measures the hardening contribution of grain boundaries, and d is the average grain size. The Hall-Petch coefficient (k) varies with the deformation mechanisms of the material [16,53]. When the average grain size of Ti–15Mo alloy is refined to 7 μm, the deformation mechanism shifts from twinning-dominated to dislocation slip-dominated. As illustrated in Fig. 14(a–d), the percentage of grains capable of twinning decreases with smaller grain sizes. To account for this change, the modified Hall-Petch equation is employed to evaluate the contribution of fine grain strengthening:

$$\sigma_g = \sigma_0 + \left[p_{twin}k_{twin} + (1 - p_{twin})k_{slip}\right]d^{-\frac{1}{2}} \tag{9}$$

where p_{twin} is the proportion of grains in which mechanical twinning occurs, k_{twin} is the Hall-Petch coefficient for twinning-dominated deformation, taken as 1112 MPa·μm$^{1/2}$[16,54], and k_{slip} is the Hall-Petch coeffient for dislocation slip-dominated deformation, taken as 234 MPa·μm$^{1/2}$ in the Ti–15Mo–1Fe alloy for estimation. When the grain sizes is small, mechanical twinning is suppressed, and the Hall-Petch coeffient reflects dislocation slip as the primary deformation mechanism.

Texture refers to the preferred orientation and can significantly affect the yield strength of the material [55]. The Ti–15Mo materials prepared by thermomechanical process exhibit notable texture. For the extruded material with an average grain size of 4 μm, the microstructure and texture are depicted in Fig. 15 (a–d), with maximum pole densities of {100}, {110}, and {111} recorded as 4.86, 10.99, and 4.89, respectively, indicating a strong texture. In contrast, the deformed material with a grain size of 7 μm has corresponding pole densities of 6.12, 8.11, and 6.25, suggesting a relatively weaker texture. While texture plays a significant role in yield strength, other factors, such as the α phase and interstitial solutes strengthening also influence material properties but are not discussed in detail here [55,56]. The contribution of various strengthening mechanisms to the yield strength are shown in Fig. 16. Notably, the contribution of grain refinement does not consistently increase as grain size decreases. However, dislocation strengthening, texture strengthening, and other factors show more substantial contributions. A summary of the contribution of dislocation strengthening, grain refinement strengthening, and texture strengthening to the yield strength of Ti–15Mo alloys is provide in Table 2.

5. Conclusions

Ti–15Mo materials with varying grain sizes were fabricated through a powder metallurgical thermomechanical process combined with simple heat treatments, and the effects of grain size on the deformation behavior and mechanical properties were systematically investigated. The main findings are as follows:

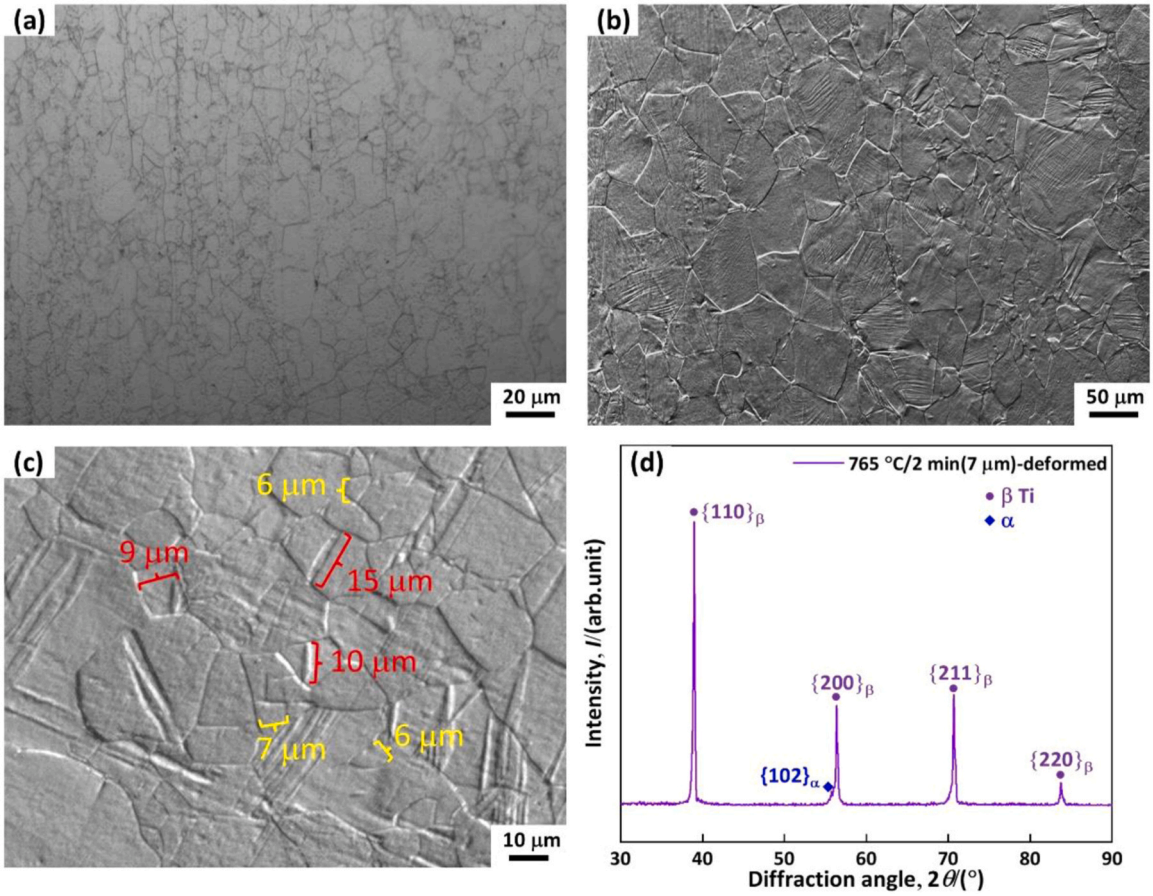

Fig. 11. (a–c) Differential interference contrast metallographs of materials with varying grain sizes : (a) 4 μm, (b) 28 μm, (c-d) 7 μm, and (d) XRD patterns of deformed Ti–15Mo alloy with an average grain size of 7 μm.

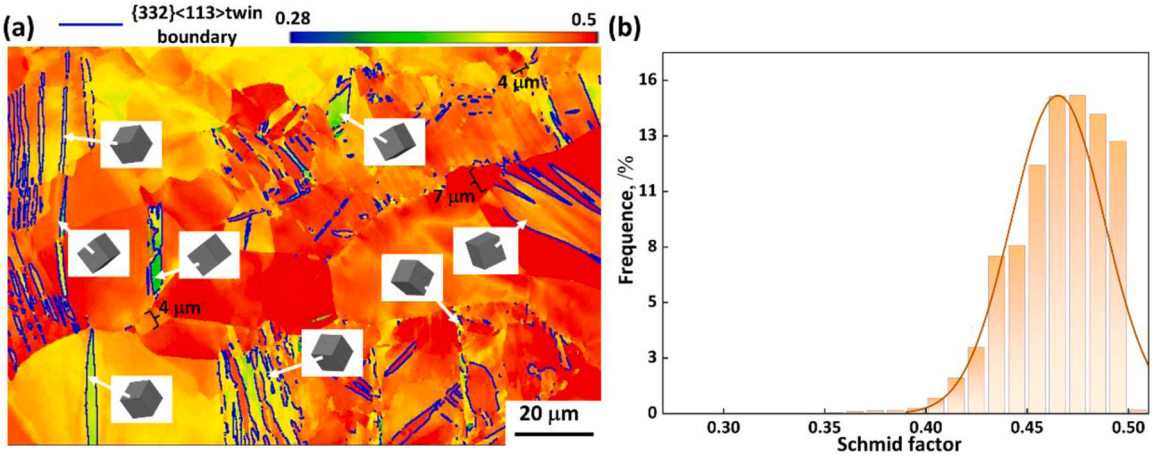

Fig. 12. (a) Schmid factor distribution and (b) statistical analysis of the Schmid factor for Ti–15Mo material with an average grain size of 7 μm after deformation.

(1) Ti–15Mo materials with grain sizes ranging from 4 to 38 μm were successfully fabricated using recycled coarse powders through thermomechanical process in powder metallurgy, combined with heat treatments.
(2) The critical grain size for suppressing the mechanical twinning is 7 μm. As the average grain size increases, the proportion of grains capable of mechanical twinning also increases.
(3) By adjusting the ratio and distribution of the grain size in Ti–15Mo materials, the Hall-Petch coefficient varies with different deformation mechanisms, enabling control over the sensitivity of yield strength to grain size and optimization of overall mechanical properties.
(4) A balance between strength and ductility can be achieved by regulating grain size. Materials with average grain size of 13 μm and 7 μm exhibit favorable comprehensive mechanical properties, with yield strengths of 715 and 921 MPa, tensile strengths of 858 and 998 MPa, and elongations of 34.4 % and 18.4 %, respectively.

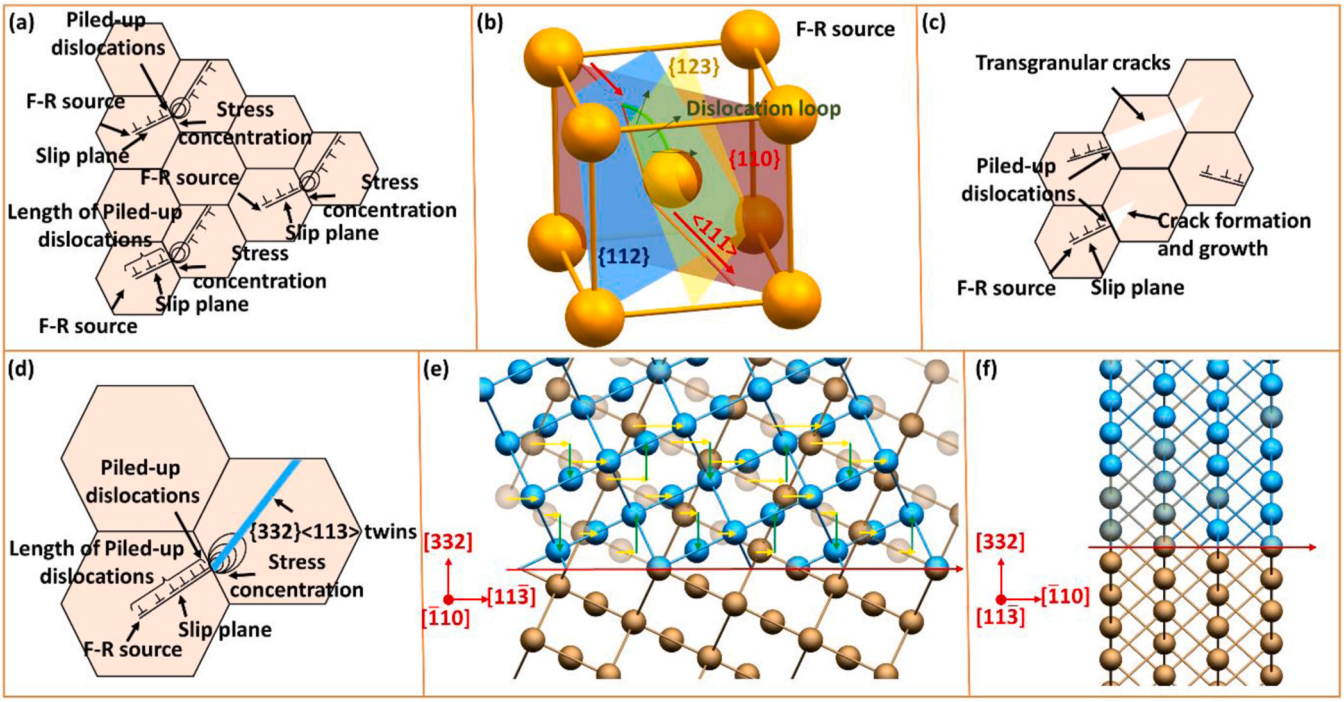

Fig. 13. Schematic illustration of the deformation evolution from dislocation slip-dominated deformation to twinning-dominated mechanisms; (a) Dislocation slip-dominated deformation behavior in small grain size, (b) dislocation multiplication by generation of dislocation loops at F-R dislocation sources, (c) dislocations pile-up at grain boundaries leading to crack nucleation and subsequent fracture, (d) twinning-dominated deformation behavior in large grain size, and (e–f) the mechanism of twinning formation in the BCC lattice.

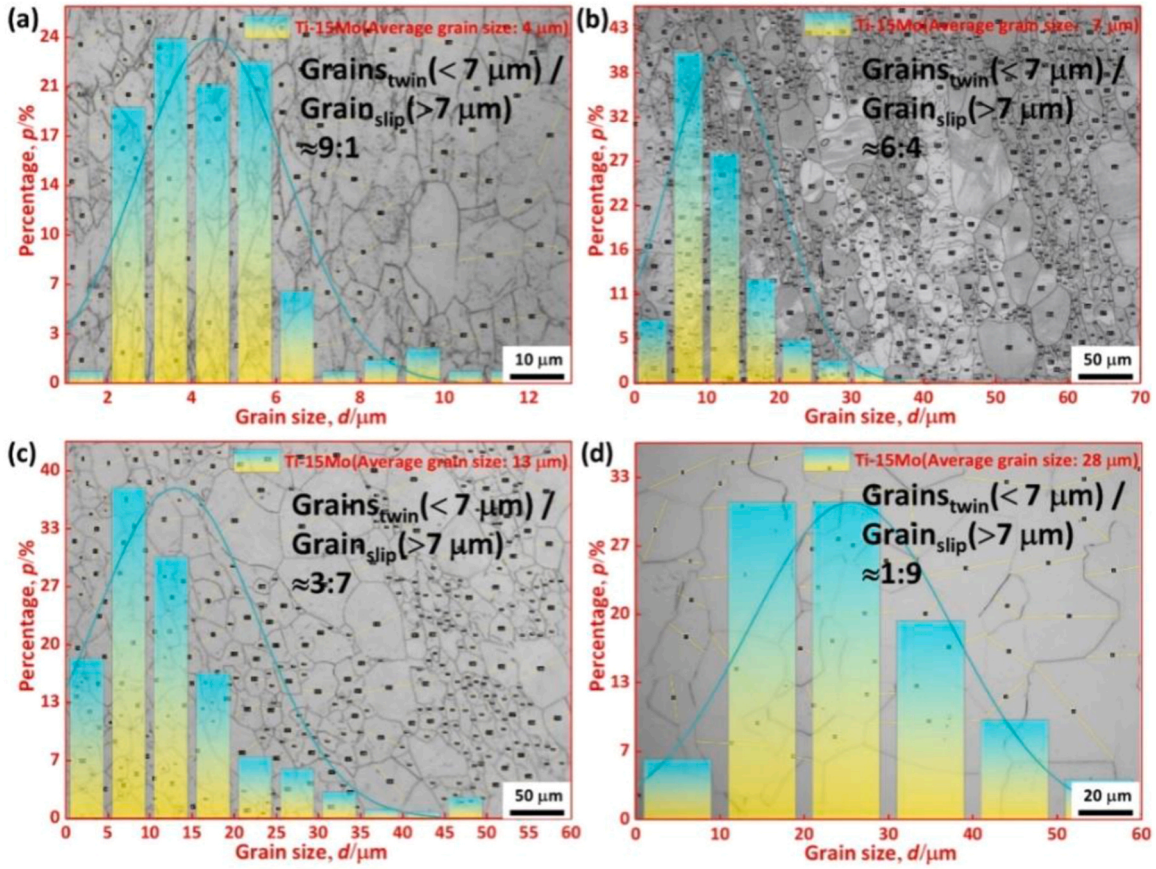

Fig. 14. Optical microstructures and corresponding grain size distribution graphs for Ti–15Mo materials with varying grain sizes: (a) 4 μm, (b) 7 μm, (c) 13 μm, and (d) 28 μm.

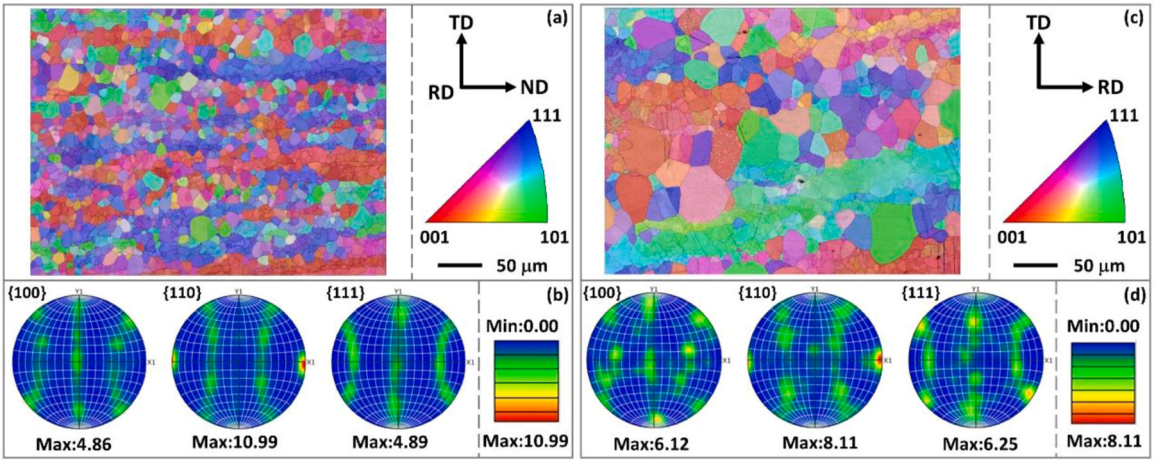

Fig. 15. EBSD phase maps and pole figures for post-defromed Ti–15Mo materials with different grain sizes: (a-b) 4 μm and (c-d) 7 μm.

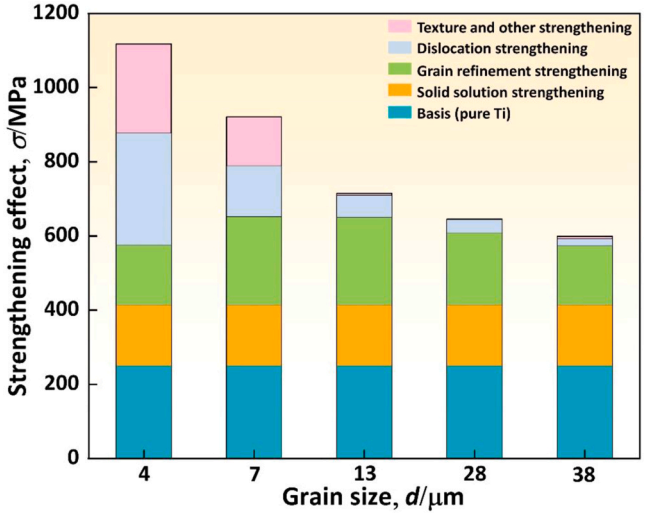

Fig. 16. Strengthening contributions of extruded Ti–15Mo materials fabricated via powder metallurgy.

Table 2
Contribution of dislocation strengthening, and grain refinement strengthening, and texture and other strengthening to the yield strength of Ti–15Mo alloys.

Grain size/ μm	Dislocation density (ρ/m^{-2})	$\Delta\sigma_d$ / MPa	$\Delta\sigma_g$ /MPa	$\Delta\sigma_{t\ and\ o}$ /MPa
4	7.05×10^{14}	302	161	241
7	1.44×10^{14}	137	238	132
13	2.81×10^{13}	60	236	5
28	1.06×10^{13}	36	194	1
38	2.86×10^{12}	19	159	7

CRediT authorship contribution statement

Nan Jia: Writing – review & editing, Validation. **Mitsuo Niinomi:** Writing – review & editing, Validation. **Deliang Zhang:** Writing – review & editing, Validation. **Xiaoli Zhao:** Writing – original draft, Supervision, Investigation, Funding acquisition. **Takayoshi Nakano:** Writing – review & editing, Validation, Funding acquisition. **Chenyang Wu:** Writing – original draft, Methodology, Investigation.

Declaration of Competing Interest

The authors declare that they have no known competing financial interests or personal relationships that could have appeared to influence the work reported in this paper.

Acknowledgement

This work was financially supported by the National Natural Science Foundation of China (Nos. 52071068, 52371097), the Major Special Projects of the Plan “Science and Technology Innovation 2025” of China (No. 2020Z060), the 111 Project, China (B16009) and JST-CREST (No. JPMJCR2194).

Data Availability

Data will be made available on request.

References

[1] M. Ahmed, D. Wexler, G. Casillas, O. Ivasishin, E. Pereloma, The influence of β phase stability on deformation mode and compressive mechanical properties of Ti–10V–3Fe–3Al alloy, Acta Mater. 84 (2015) 124–135, https://doi.org/10.1016/j.actamat.2014.10.043.
[2] E. Awannegbe, H. Li, T. Song, F. Niessen, M. Qian, A. Gazder, M. Nancarrow, E. Pereloma, Microstructural characterisation and mechanical evaluation of Ti–15Mo manufactured by laser metal deposition, J. Alloy. Compd. 947 (2023) 169553, https://doi.org/10.1016/j.jallcom.2023.169553.
[3] M. Yan, M. Qian, C. Kong, M. Dargusch, Impacts of trace carbon on the microstructure of as-sintered biomedical Ti–15Mo alloy and reassessment of the maximum carbon limit, Acta Biomater. 10 (2014) 1014–1023, https://doi.org/10.1016/j.actbio.2013.10.034.
[4] X. Min, X. Chen, S. Emura, K. Tsuchiya, Mechanism of twinning-induced plasticity in β-type Ti–15Mo alloy, Scr. Mater. 69 (2013) 393–396, https://doi.org/10.1016/j.scriptamat.2013.05.027.
[5] X. Min, S. Emura, N. Sekido, T. Nishimura, K. Tsuchiya, K. Tsuzaki, Effects of Fe addition on tensile deformation mode and crevice corrosion resistance in Ti–15Mo alloy, Mater. Sci. Eng.: A 527 (2010) 2693–2701, https://doi.org/10.1016/j.msea.2009.12.050.
[6] A. Almeida, D. Gupta, C. Loable, R. Vilar, Laser-assisted synthesis of Ti–Mo alloys for biomedical applications, Mater. Sci. Eng.: C. 32 (2012) 1190–1195, https://doi.org/10.1016/j.msec.2012.03.007.
[7] Y. Li, S. Liu, J. Wu, W. Du, G. Qin, E. Zhang, Effect of anodic oxidation on the corrosion resistance and antibacterial properties of Ti–15Mo–9Ag for biomedical application, Surf. Coat. Technol. 472 (2023) 129948, https://doi.org/10.1016/j.surfcoat.2023.129948.
[8] K. Zhao, X. Zhou, T. Hu, Y. Li, Z. Ye, F. Zhang, M. Wang, H. Tan, Microstructure characterization and tensile properties of Ti–15Mo alloy formed by directed energy deposition, Mater. Sci. Eng.: A 858 (2022) 144103, https://doi.org/10.1016/j.msea.2022.144103.
[9] X. Min, K. Tsuzaki, S. Emura, K. Tsuchiya, Enhanced uniform elongation by pre-straining with deformation twinning in high-strength β-titanium alloys with an isothermal ω-phase, Philos. Mag. Lett. 92 (2012) 726–732, https://doi.org/10.1080/09500839.2012.725949.
[10] H. Wang, D. Lai, C. Song, Y. Zhao, J. Cheng, M. Bönisch, Z. Sun, Zero thermal expansion and high Young's modulus in Ti–Nb achieved by concurrent α''_{iso} and ω precipitation, Scr. Mater. 232 (2023) 115477, https://doi.org/10.1016/j.scriptamat.2023.115477.

[11] P. Dobroň, F. Chmelík, S. Yi, K. Parfenenko, D. Letzig, J. Bohlen, Grain size effects on deformation twinning in an extruded magnesium alloy tested in compression, Scr. Mater. 65 (2011) 424–427, https://doi.org/10.1016/j.scriptamat.2011.05.027.
[12] R. Zheng, J. Du, S. Gao, H. Somekawa, S. Ogata, N. Tsuji, Transition of dominant deformation mode in bulk polycrystalline pure Mg by ultra-grain refinement down to sub-micrometer, Acta Mater. 198 (2020), https://doi.org/10.1016/j.actamat.2020.07.055.
[13] R. Ueji, N. Tsuchida, D. Terada, N. Tsuji, Y. Tanaka, A. Takemura, K. Kunishige, Tensile properties and twinning behavior of high manganese austenitic steel with fine-grained structure, Scr. Mater. 59 (2008) 963–966, https://doi.org/10.1016/j.scriptamat.2008.06.050.
[14] S. Kang, J. Jung, M. Kang, W. Woo, Y. Lee, The effects of grain size on yielding, strain hardening, and mechanical twinning in Fe–18Mn–0.6C–1.5Al twinning-induced plasticity steel, Mater. Sci. Eng.: A 652 (2016) 212–220, https://doi.org/10.1016/j.msea.2015.11.096.
[15] H. Xu, Z. Li, A. Dong, H. Xing, D. Du, L. He, H. Peng, G. Zhu, D. Wang, B. Sun, Selective laser melting of biomedical Ti15Mo alloy: a proper combination of strength and ductility under the effects of multiple mechanisms, J. Alloy. Compd. 873 (2021) 159686, https://doi.org/10.1016/j.jallcom.2021.159686.
[16] K. Yao, X. Min, Static and dynamic Hall-Petch relations in {332} TWIP Ti–15Mo alloy, Mater. Sci. Eng.: A 827 (2021) 142044, https://doi.org/10.1016/j.msea.2021.142044.
[17] S. Zherebtsov, M. Ozerov, M. Klimova, D. Moskovskikh, N. Stepanov, G. Salishchev, Mechanical behavior and microstructure evolution of a Ti–15Mo/TiB titanium–matrix composite during hot deformation, Metals 9 (2019) 1175, https://doi.org/10.3390/met9111175.
[18] K. Zhao, X. Zhou, T. Hu, Y. Li, Z. Ye, F. Zhang, M. Wang, H. Tan, Microstructure characterization and tensile properties of Ti–15Mo alloy formed by directed energy deposition, Mater. Sci. Eng.: A 858 (2022) 144103, https://doi.org/10.1016/j.msea.2022.144103.
[19] S. El-Soudani, Powder-based titanium alloys: properties and selection, Titan. Powder Metall. 25 (2015) 469–496, https://doi.org/10.1016/B978-0-12-800054-0.00025-3.
[20] T. Chen, C. Suryanarayana, C. Yang, Advanced titanium materials processed from titanium hydride powder, Powder Technol. 423 (2023) 118504, https://doi.org/10.1016/j.powtec.2023.118504.
[21] E. Awannegbe, H. Li, T. Song, F. Niessen, M. Qian, A. Gazder, M. Nancarrow, E. Pereloma, Microstructural characterisation and mechanical evaluation of Ti–15Mo manufactured by laser metal deposition, J. Alloy. Compd. 947 (2023) 169553, https://doi.org/10.1016/j.jallcom.2023.169553.
[22] T. Li, F. Zhou, L. Long, B. Wang, Z. Tang, X. Li, Fatigue crack growth and mechanical properties of laminated TC4/TB8 titanium alloys fabricated by diffusion bonding, Mater. Charact. 200 (2023) 112825, https://doi.org/10.1016/j.matchar.2023.112825.
[23] X. Min, S. Emura, N. Sekido, T. Nishimura, K. Tsuchiya, K. Tsuzaki, Effects of Fe addition on tensile deformation mode and crevice corrosion resistance in Ti–15Mo alloy, Mater. Sci. Eng.: A 527 (2010) 2693–2701, https://doi.org/10.1016/j.msea.2009.12.050.
[24] L. Xiang, X. Min, Effect of {332} twins combined with isothermal ω-phase on mechanical properties in Ti–15Mo alloy with different oxygen contents, Acta Met. Sin. 54 (2018) 1262–1272, https://doi.org/10.11900/0412.1961.2018.00022.
[25] J. Xu, K. Li, J. Tang, Y. Zhou, J. Luo, W. Tang, Y. Lai, M. Dargusch, M. Yan, Additive manufacturing of anti-bacterial and low-cost Ti–Mo(–Ag) alloys using elemental powders through in situ laser alloying, J. Mater. Sci. 58 (2023) 2268–2293, https://doi.org/10.1007/s10853-022-08107-6.
[26] S. Xu, C. Zhou, Y. Liu, B. Liu, K. Li, Microstructure and mechanical properties of Ti–15Mo–xTiC composites fabricated by in-situ reactive sintering and hot swaging, J. Alloy. Compd. 738 (2018) 188–196, https://doi.org/10.1016/j.jallcom.2017.12.124.
[27] K. Yao, X. Min, Static and dynamic Hall-Petch relations in {332}<113> TWIP Ti–15Mo alloy, Mater. Sci. Eng.: A 827 (2021) 142044, https://doi.org/10.1016/j.msea.2021.142044.
[28] K. Yao, S. Xin, Y. Yang, Y. Du, J. Dai, T. Li, X. Min, Ultrahigh cryogenic strength and exceptional ductility at 20 K in a TWIP Ti–15Mo alloy, Scr. Mater. 213 (2022) 114595, https://doi.org/10.1016/j.scriptamat.2022.114595.
[29] K. Zhao, X. Zhou, T. Hu, Y. Li, Z. Ye, F. Zhang, M. Wang, H. Tan, Microstructure characterization and tensile properties of Ti–15Mo alloy formed by directed energy deposition, Mater. Sci. Eng.: A 858 (2022) 144103, https://doi.org/10.1016/j.msea.2022.144103.
[30] L. Zhou, J. Sun, J. Chen, W. Chen, Y. Ren, Y. Niu, C. Li, W. Qiu, Study of substrate preheating on the microstructure and mechanical performance of Ti–15Mo alloy processed by selective laser melting, J. Alloy. Compd. 928 (2022) 167130, https://doi.org/10.1016/j.jallcom.2022.167130.
[31] L. Sun, Z. Xu, L. Peng, X. Lai, Effect of grain size on the ductile-brittle fracture behavior of commercially pure titanium sheet metals, Mater. Sci. Eng.: A 822 (2021) 141630, https://doi.org/10.1016/j.msea.2021.141630.
[32] B. Margolin, V. Fomenko, V. Shvetsova, F. Shishkov, E. Yurchenko, The plastic strain effect on cleavage microcracks propagation, Eng. Fract. Mech. 290 (2023) 109446, https://doi.org/10.1016/j.engfracmech.2023.109446.
[33] Y. Zhang, J. Wang, Microcrack nucleation and propagation investigation ofInconel 740H alloy under in situhigh temperature tensile test, Acta Met. Sin. 53 (2017) 1627–1635, https://doi.org/10.11900/0412.1961.2017.00218.
[34] M. Ding, T. Wang, B. Maerz, S. Robertson, Z. Sun, L. Fan, Y. Shi, H. Wu, Formation of twins in AlON material and its effects on the Vickers hardness and fracture toughness, Ceram. Int. 45 (2019) 21127–21135, https://doi.org/10.1016/j.ceramint.2019.07.089.
[35] G. Schaffar, D. Tscharnuter, V. Maier–Kiener, Exploring the high-temperature deformation behavior of monocrystalline silicon–An advanced nanoindentation study, Mater. Des. 233 (2023) 112198, https://doi.org/10.1016/j.matdes.2023.112198.
[36] P. Guo, F. Li, L. Yang, R. Bagheri, Q. Zhang, B. Li, K. Cho, Z. Song, W. Sun, H. Liu, Ultra-fine-grained Zn–0.5Mn alloy processed by multi-pass hot extrusion: grain refinement mechanism and room-temperature superplasticity, Mater. Sci. Eng.: A 748 (2019) 262–266, https://doi.org/10.1016/j.msea.2019.01.089.
[37] G. Wu, Y. Lin, M. Chen, W. Qiu, N. Zeng, S. Zhang, M. Wan, D. He, Y. Jiang, M. Naseri, Continuous dynamic recrystallization behaviors in a single-phase deformed Ti–55511 alloy by cellular automata model, J. Alloy. Compd. 1002 (2024) 175293, https://doi.org/10.1016/j.jallcom.2024.175293.
[38] W. Wang, X. Wang, W. Mei, J. Sun, Role of grain size in tensile behavior in twinning-induced plasticity β Ti–20V–2Nb–2Zr alloy, Mater. Charact. 120 (2016) 263–267, https://doi.org/10.1016/j.matchar.2016.09.016.
[39] Y. Im, Y. Lee, H. Park, K. Song, Effect of the initial grain size and orientation on the formation of deformation twins in Ti–15Mo alloy, J. Mater. Sci. 52 (2017) 11668–11674, https://doi.org/10.1007/s10853-017-1314-0.
[40] L. Lilensten, F. Sun, A. Hocini, G. Dirras, P. Vermaut, F. Prima, {332}<113> mechanical detwinning as a deformation mechanism in the β-metastable Ti–15Mo alloy during cyclic loading, Scr. Mater. 232 (2023) 115503, https://doi.org/10.1016/j.scriptamat.2023.115503.
[41] X. Min, K. Tsuzaki, S. Emura, T. Sawaguchi, S. Ii, K. Tsuchiya, {332}<113> Twinning system selection in a β-type Ti–15Mo–5Zr polycrystalline alloy, Mater. Sci. Eng.: A 579 (2013) 164–169, https://doi.org/10.1016/j.msea.2013.04.119.
[42] X. Zhao, Y. Wang, H. Xue, N. Jia, Y. Liu, D. Zhang, The effect of strain rate on deformation-induced α″ phase transformation and mechanical properties of a metastable β-type Ti–30Zr–5Mo alloy, J. Alloy. Compd. 894 (2022) 162394, https://doi.org/10.1016/j.jallcom.2021.162394.
[43] R. Gholizadeh, A. Shibata, N. Tsuji, Grain refinement mechanisms in BCC ferritic steel and FCC austenitic steel highly deformed under different temperatures and strain rates, Mater. Sci. Eng.: A 790 (2020) 139708, https://doi.org/10.1016/j.msea.2020.139708.
[44] Z. He, Y. Zhang, J. Liang, Y. Li, Quantitative investigation on the individual contribution of twinning and dislocation slip to creep in dilute Mg–Y alloys with various grain sizes, J. Alloy. Compd. 990 (2024) 174473, https://doi.org/10.1016/j.jallcom.2024.174473.
[45] X. Ye, B. Chen, J. Shen, J. Umeda, K. Kondoh, Microstructure and strengthening mechanism of ultrastrong and ductile Ti–xSn alloy processed by powder metallurgy, J. Alloy. Compd. 709 (2017) 381–393, https://doi.org/10.1016/j.jallcom.2017.03.171.
[46] M. Najafizadeh, A. Bahadoran, M. Bozorg, B. Sadeghi, J. Liang, D. Zhang, Microstructures and mechanical properties of high strength Ti–XAl–2Fe–3Cu alloys fabricated by powder compact extrusion, J. Alloy. Compd. 884 (2021) 161136, https://doi.org/10.1016/j.jallcom.2021.161136.
[47] K. Chia, K. Jung, H. Conrad, Dislocation density model for the effect of grain size on the flow stress of a Ti–15.2 at% Mo β-alloy at 4.2–650 K, Mater. Sci. Eng.: A 409 (2005) 32–38, https://doi.org/10.1016/j.msea.2005.03.117.
[48] S. Sahoo, V. Hiwarkar, A. Majumdar, I. Samajdar, P. Pant, G. Dey, D. Srivastav, R. Tiwari, S. Banerjee, Presence and absence of significant twinning: effects on cold deformed microstructures of single phase Zircaloy 2, Mater. Sci. Eng.: A 518 (2009) 47–55, https://doi.org/10.1016/j.msea.2009.05.025.
[49] 2013, Precipitate characteristics and their effect on the prismatic-slip-dominated deformation behaviour of an Mg–6 Zn alloy, Acta Materialia 61 (2013) 4091–4102. https://doi.org/10.1016/j.actamat.2013.03.033.
[50] S. Xu, C. Zhou, Y. Liu, B. Liu, K. Li, Microstructure and mechanical properties of Ti–15Mo–xTiC composites fabricated by in-situ reactive sintering and hot swaging, J. Alloy. Compd. 738 (2018) 188–196, https://doi.org/10.1016/j.jallcom.2017.12.124.
[51] X. Ye, B. Chen, J. Shen, J. Umeda, K. Kondoh, Microstructure and strengthening mechanism of ultrastrong and ductile Ti–xSn alloy processed by powder metallurgy, J. Alloy. Compd. 709 (2017) 381–393, https://doi.org/10.1016/j.jallcom.2017.03.171.
[52] Z. Gan, Y. He, D. Liu, B. Zhang, L. Shen, Hall-Petch effect and strain gradient effect in the torsion of thin gold wires, Scr. Mater. 87 (2014) 41–44, https://doi.org/10.1016/j.scriptamat.2014.05.011.
[53] C. Wu, X. Zhao, M. Zhang, H. Hosoda, T. Nakano, M. Niinomi, N. Jia, Z. Shao, D. Zhang, Strong grain size effect on tensile behavior of the body-centered-cubic Ti–30Zr–5Mo alloy with stress-induced α″ martensitic transformation, Mater. Sci. Eng.: A 900 (2024) 146455, https://doi.org/10.1016/j.msea.2024.146455.
[54] K. Yao, X. Min, S. Emura, F. Meng, X. Ji, K. Tsuchiya, Enhancement of impact toughness of β-type Ti–Mo alloy by {332}<113> twinning, J. Mater. Sci. 54 (2019) 11279–11291, https://doi.org/10.1007/s10853-019-03679-2.
[55] F. Guo, H. Yu, C. Wu, Y. Xin, C. He, Q. Liu, The mechanism for the different effects of texture on yield strength and hardness of Mg alloys, Sci. Rep. 7 (2017) 8647, https://doi.org/10.1038/s41598-017-08966-z.
[56] X. Guo, Z. Chu, D. Shao, P. Li, B. Wu, Wire-arc directed energy deposition of Ti–6Al–4V alloy using CO_2 active interpass cooling: phase composition, grain orientation, texture strength, dislocation density and mechanical property, J. Mater. Res. Technol. 28 (2024) 3196–3206, https://doi.org/10.1016/j.jmrt.2023.12.262.